

# Journal of Biomedical Optics

[SPIEDigitalLibrary.org/jbo](http://SPIEDigitalLibrary.org/jbo)

## **Improving limited-projection-angle fluorescence molecular tomography using a co-registered x-ray computed tomography scan**

Karin Radrich  
Angelique Ale  
Vladimir Ermolayev  
Vasilis Ntziachristos

# Improving limited-projection-angle fluorescence molecular tomography using a co-registered x-ray computed tomography scan

Karin Radrich,<sup>a,b</sup> Angelique Ale,<sup>a,b</sup> Vladimir Ermolayev,<sup>a,b</sup> and Vasilis Ntziachristos<sup>a,b</sup>

<sup>a</sup>Institute for Biological and Medical Imaging, Helmholtz Zentrum München, Ingolstädter Landstraße 1, 85764 Neuherberg, Germany

<sup>b</sup>Technische Universität München, Chair for Biological Imaging, Ismaninger Straße 22, 81675 München, Germany

**Abstract.** We examine the improvement in imaging performance, such as axial resolution and signal localization, when employing limited-projection-angle fluorescence molecular tomography (FMT) together with x-ray computed tomography (XCT) measurements versus stand-alone FMT. For this purpose, we employed living mice, bearing a spontaneous lung tumor model, and imaged them with FMT and XCT under identical geometrical conditions using fluorescent probes for cancer targeting. The XCT data was employed, herein, as structural prior information to guide the FMT reconstruction. Gold standard images were provided by fluorescence images of mouse cryoslices, providing the ground truth in fluorescence bio-distribution. Upon comparison of FMT images versus images reconstructed using hybrid FMT and XCT data, we demonstrate marked improvements in image accuracy. This work relates to currently disseminated FMT systems, using limited projection scans, and can be employed to enhance their performance. © 2012 Society of Photo-Optical Instrumentation Engineers (SPIE). [DOI: 10.1117/1.JBO.17.12.126011]

Keywords: fluorescence molecular tomography; x-ray computed tomography; co-registration; multimodality; molecular imaging; hybrid imaging; priors; reconstruction.

Paper 12378 received Jun. 18, 2012; revised manuscript received Oct. 30, 2012; accepted for publication Nov. 9, 2012; published online Dec. 4, 2012.

## 1 Introduction

Fluorescence molecular tomography (FMT) is a method that images tissue biomarkers by resolving the bio-distribution of fluorescently labeled agents.<sup>1-6</sup> By utilizing agents that target functional and molecular tissue parameters, FMT can enable highly diverse applications such as cancer, cardiac, inflammation or neurodegenerative imaging.<sup>7-10</sup> One of the strengths of FMT is the use of nonionizing energy, typically, in the near-infrared range of the optical spectrum. An additional advantage is the ability to resolve many tracers, simultaneously, by using fluorescent labels at different wavelengths. Conversely, the most important limitation is the diffusive character of near infrared photons that propagate in tissues which complicates image formation and quantification and limits the size (depth) of the object that can be imaged, typically to a few centimeters.<sup>11,12</sup>

The development of quantitative image reconstruction methods and free-space charge-coupled device (CCD) camera based detection, have yielded practical implementations for optical tomography.<sup>13-16</sup> Most tomographic implementations, reported so far, operate as stand-alone systems. However, the combination of optical tomography approaches with other modalities, in particular modalities yielding anatomical information, such as magnetic resonance imaging (MRI) or x-ray computed tomography (XCT), can improve image reconstruction performance.<sup>17-19</sup> Improvements can be delivered by utilizing the anatomical information as prior information to limit the uncertainty of the tomographic problem.<sup>20-25</sup> Typically, knowledge about the

internal structures of an animal, such as the segmentation of different tissue types like bones, lung, heart, and brain allows the assignment of different optical properties to each of these tissues and consequently, more appropriate modeling of photon propagation inside each tissue type. A similar practice is employed in positron emission tomography (PET), whereby, information on density differences from XCT scans is used for attenuation correction resulting in superior PET reconstructions.<sup>26</sup> Yet, it is even more crucial in FMT inversions due to the stronger dependence of near-infrared (NIR) photons on the tissue optical properties.<sup>27</sup> In addition, the anatomical information can be used to define functionals that can be employed in the reconstruction process to restrict the ill-posed nature of the inverse problem and stabilize the performance of the method.<sup>22,24</sup>

The use of priors from an anatomical modality in optical tomography of tissues has been demonstrated in the past. As early as 1995, Barbour et al. examined, theoretically, the potential utility of incorporating magnetic resonance (MR)-derived anatomical image data to enhance the quality of tomographic optical imaging in order get over the hurdle imposed by the diffusive character of light propagation in tissue.<sup>24</sup> Their approach consisted in simulating measurements for segmented three-dimensional (3-D) MR data sets of breast tissue in which different tissue types were assigned different optical properties. Consequently, the dependence of image quality on different properties, also related to the reconstruction algorithms, could be investigated. At that time, optical tomography, with or without priors, was still in its infancy. Nevertheless, the simulations, presented in this early work, showed promise to the feasibility of recovering relevant information from optical measurements and

---

Address all correspondence to: Vasilis Ntziachristos, Helmholtz Zentrum München, Institute for Biological and Medical Imaging, Ingolstädter Landstraße 1, 85764 Neuherberg, Germany. Tel: +49 (0)89 3187 3852; Fax: +49 (0) 89 3187 3008; E-mail: [v.ntziachristos@tum.de](mailto:v.ntziachristos@tum.de)

lead on the right track for further hardware and software developments.

Additional methodological approaches incorporating priors in optical tomography and implementations that combined diffuse optical tomography (DOT) or FMT with MRI, ultrasound or x-ray CT were since proposed.<sup>17,23,28–33</sup> Pogue et al. and Pogue and Paulsen, for instance, examined a reconstruction algorithm that would take advantage of the data available from a composite MRI-near-infrared spectroscopy (NIRS) system for imaging the rat cranium.<sup>17,28</sup> They tested its ability to obtain high-spatial-resolution images of the near-infrared optical absorption coefficient in simulations and were able to distinguish even local perturbations located inside one tissue type. Intes et al. used a different approach to incorporate prior information.<sup>29</sup> Their algorithm was based on a Bayesian framework with a spatially varying *a priori* probability density function extracted from MRI anatomical maps and the additional incorporation of physiological priors. Furthermore, x-ray mammography was the anatomical modality of choice with Li et al., which included a modified Tikhonov regularization method in the DOT reconstruction.<sup>30</sup> They explored the usage of two different types of priors that combined the L-curve approach for finding one parameter with a signal-to-noise ratio type of maximization for the second. Their simulations showed promising results for contrast-to-noise ratio and resolution improvement. On the instrumentation front, Gulsen et al.<sup>31</sup> presented a combined DOT and MRI system for small animal imaging, whereby, a similar approach was also considered in clinical studies.<sup>34</sup> Ultrasound and optical tomography was combined in a handheld device by Zhu et al.<sup>32</sup>

The combination of FMT with anatomical devices has also been investigated. Davis et al., for instance, incorporated a fluorescence imaging system directly into a clinical MRI to improve detection of brain tumors in mice.<sup>35</sup> The regularization was based on segmented MR images and a Laplacian-type regularization matrix that had been introduced in Ref. 22. The potential gain from integrating MRI and FMT has been realized by several groups and is currently one major focus of hybrid FMT research.<sup>36</sup> FMT has also been recently combined with x-ray CT in a hybrid animal imaging system based on free-space CCD camera photon collection.<sup>19</sup> This approach enabled the collection of high spatial-sampling data at 360 deg projections. The integration of the optical hardware onto the gantry of a micro-CT device allowed accurate co-registration of FMT and XCT images. Similar approaches fixed the acquisition system and rotated the animal.<sup>37,38</sup> Different reconstruction schemes incorporating XCT anatomical data were investigated both for the forward problem.<sup>39</sup> and for the inverse part.<sup>19,33,40,41</sup> Ale et al., for instance, compared different regularization methods, based on Tikhonov, Laplace, and different weighting of segments, and concluded, from simulations and *ex vivo* experiments, that the latter approach was the most promising.<sup>40</sup> Hyde et al. used a similar approach employing different weights but, additionally, focused on the development of data driven regularization and investigated the influence of subdivision of anatomical segments on the reconstruction outcome.<sup>41</sup>

The work described above is not meant as an exhaustive review of work in the field of hybrid optical systems, but only as an indication of significant prior research in the subject matter of this paper.

Despite the wealth of hybrid approaches considered for experimental optical tomography prototypes, most fluorescence

tomography systems that have been disseminated to the laboratory operate as limited-projection-angle stand-alone systems, i.e., more specifically acquiring optical projections from a bounded slab geometry.<sup>10,42–46</sup> Compared to a 360 deg projection system, the slab geometry is technically easier to implement and comes with several operational advantages including easy animal placement, shorter experimentation times, and offers systems of reduced cost. Conversely, the slab geometry attains imaging performance limitations because it offers limited resolution along the axis of the projections.<sup>37,45</sup> This geometry also offers the possibility to develop rigid animal holders that can be translated between different modalities for obtaining hybrid data.<sup>47</sup> While the benefit of such translation possibility has been used to compare FMT and anatomical images, no investigation, so far, has examined the improvements offered when incorporating anatomical information into data acquired from animal models of disease *in vivo*.

In this work we, therefore, investigated the improvement achieved in the imaging performance of limited-projection-angle (slab geometry) FMT systems when incorporating hybrid anatomical information *in vivo*. Co-registration was achieved by means of an animal cartridge that can offer rigid animal translation between a stand-alone FMT scanner and a XCT animal micro-scanner. The work relates to improving the overall performance achieved by limited-projection-angle FMT systems, by employing algorithmic improvements, as long as an anatomical imaging modality is also available.

## 2 Methods

### 2.1 Data Acquisition

#### 2.1.1 X-ray CT imaging

For anatomical imaging, a small animal x-ray CT (Inveon, Siemens Preclinical Solutions, Knoxville, Tennessee) was used. The imaging protocol, for the experiments conducted in this study, was set to acquire a 3-D data set at an effective resolution of 103.58  $\mu\text{m}$  after fourfold binning. The x-ray CT source operated at 80 kV and 500  $\mu\text{A}$  with an exposure time of 200 ms for each of the 360 acquired projections. The 3-D CT data was post-processed to account for beam hardening and exported in digital imaging and communications in medicine (DICOM) format for further processing.

#### 2.1.2 FMT imaging

For fluorescence tomography, a limited-projection-angle, trans-illumination tomography system (FMT 2500, VisEn Medical, Woburn, Massachusetts) was used. Data was collected at the 700 to 730 nm fluorophore emission wavelength range in response to a 680 nm laser source being scanned over the region of interest. Typical scan patterns assumed on average a 13  $\times$  6 grid (36 mm  $\times$  15 mm) leading to 78 points. For each point scanned, trans-illumination images were collected at the emission and the excitation wavelengths. White light mouse photographs were also collected and served as the basis for co-registration, as described in the following paragraph.

Exposure times and laser power information were recorded and employed to scale the intensities in the fluorescence and intrinsic images. The reconstructed fluorescence signal distribution, computed by the stand-alone FMT device with an isotropic resolution of 1 mm, was exported in DICOM format and

overlaid to the XCT volume by fiducial mapping using the software package AMIRA (Visage Imaging GmbH, Berlin, Germany). This post-reconstruction overlay was used to compare and validate the results attained with the pre-reconstruction overlay.

## 2.2 Co-Registration of FMT and XCT

Co-registration was achieved by means of an imaging cartridge (FMT 2500, VisEn Medical, Woburn, Massachusetts) shown on Fig. 1. The transparent plates are made of glass-reinforced extruded nylon and covered with an anti-reflection coating for the NIR. The anaesthetized animal was inserted between the two transparent plates which apply mild compression to the mouse body. In this manner, the animal stayed immobile in the same position, while sequentially imaged by FMT and XCT. Figure 1(a) shows the transversal schematic view of such a compressed object and the general imaging setup geometry.

The cartridge was always inserted in the same horizontal position in the FMT system, by means of rigid rails, while it also contained fiducial markers [Fig. 1(b), arrows] consisting of small cavities in the frame which were visible in the x-ray CT images. The fiducial markers are manufactured to mark a plane that is parallel to the detection plane of the CCD camera and were employed to track the position of the cartridge when inserted into the XCT bore so that FMT and XCT data could be accurately co-registered.

For registration purposes, information from the fiducial markers was combined with boundary information of the

animal, as seen on XCT images and the animal photographs obtained by the FMT system, and guided the translation and rotation of the reconstructed 3-D XCT volume to fit in a common coordinate system with the FMT data. A schematic of this concept can be seen in Fig. 1(c). The white light image, taken in the FMT device, defined the coordinate system to which the XCT volume had to be co-registered. Since, however, the XCT information is 3-D and the photograph is two-dimensional (2-D), it was not possible to directly extract information on possible rotation of the cartridge in the XCT system, but the plane defined by the fiducial markers was considered as the horizontal plane corresponding to the photograph. The fiducial markers were then employed to measure, and correct, for the rotation angle between the  $x$ -,  $y$ -, and  $z$ -axis in XCT and FMT. After rotation,  $x$ - $y$  translation was applied to align the XCT images and FMT data to a common coordinate system. More specifically, the orientation of the cassette (transversal, sagittal plane) was extracted from the reconstructed XCT images based on the cassette plates and fiducial markers. According to Fig. 1, the angles denoted by  $\alpha$ ,  $\beta$ ,  $\gamma$  between the XCT planes ( $x_{\text{xct}}$ ,  $y_{\text{xct}}$ ,  $z_{\text{xct}}$ ) and the ( $x_{\text{fmt}}$ ,  $y_{\text{fmt}}$ ,  $z_{\text{fmt}}$ ) plane of the photograph from the FMT device were computed by projecting the FMT photograph to the  $x_{\text{xct}}$ - $y_{\text{xct}}$  ( $z_{\text{xct}} = 0$ ) plane and computing the angles between this plane and the ones defined by the fiducial markers along the transversal and sagittal slices. Then, the 3-D XCT image was rotated so that it could be aligned with the ( $x_{\text{fmt}}$ ,  $y_{\text{fmt}}$ ,  $z_{\text{fmt}}$ ) plane. Having consequently produced two parallel data sets, a translation step was then performed to map the boundary and fiducial information from the XCT to the

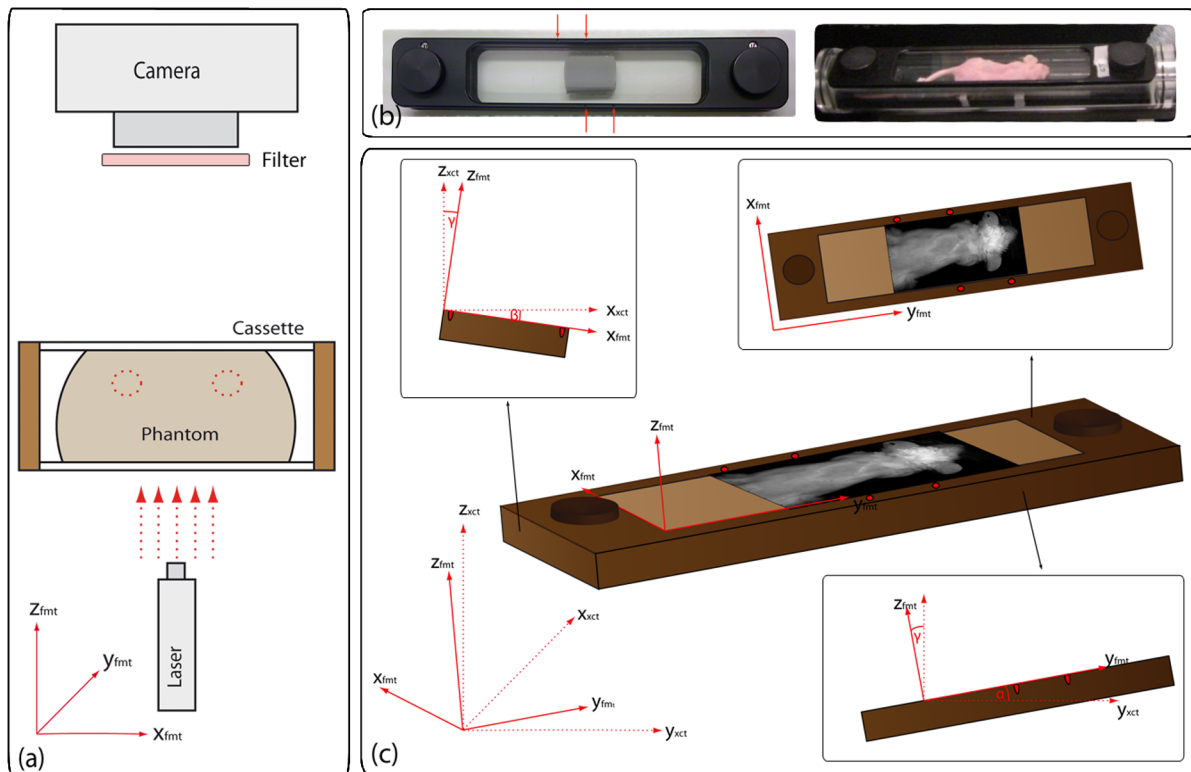


**Fig. 1** FMT system and mouse bed geometry and orientation: (a) schematic of a limited-projection-angle FMT system (not in right scale): a laser is scanning along the  $x$ - and  $y$ -axis and a camera is acquiring the trans-illumination images for each scan. (b) Imaging cartridge containing the phantom (left) and a mouse (right). Small holes in the nontransparent margin of the cartridge serve as fiducial markers (arrows). (c) The coordinate systems of XCT and FMT, respectively, are mapped to each other through rotation and translation.

mouse photograph. To achieve this, the animal boundary from the XCT was produced by projecting the XCT slices along the  $z$ -axis on one single plane that corresponded to the FMT photographic plane (i.e., a maximum intensity projection and subsequent boundary extraction by thresholding). This step is visualized in Fig. 2 (see also the results section). Therefore, in contrast to previous FMT-XCT co-registration approaches, mapping 3-D data sets to each other using fiducial markers placed on a cartridge, the approach herein performed 2-D to 3-D mapping and employed fiducial and boundary markers for improving the accuracy of the co-registration.<sup>47</sup>

The width dimension ( $z$ ) of the animal was obtained from the XCT and confirmed by the internal measurement system in the FMT device which measures the cassette width using two ultrasound transducers. The accuracy of the co-registration method was examined using a 230  $\mu\text{m}$  copper wire placed in random directions in the cartridge and imaged by XCT and FMT (only reflectance image). All calculations were performed with a custom made algorithm implemented in Matlab (Mathworks Inc., Massachusetts).

### 2.3 Image Segmentation

Segmentation of the XCT data was performed to single out different anatomical structures. For imaging the upper mouse thorax, 4 organs were typically segmented such as the lung, bone, heart, and remaining tissue. The segmentation was performed automatically using thresholding, seed growing, and signal detection algorithms as previously reported by Freyer et al.<sup>48</sup>

Summarized, because of the high contrast, bone segmentation could be performed using an automatically derived threshold. From this first segmentation, the ribcage was obtained and used for localization of the lung which was finally segmented using a seed growing algorithm. The seed points were automatically determined from an intensity histogram of voxels lying inside the region of interest determined by the ribcage. For the segmentation of the heart, a shape model was used that was iteratively adjusted based on the ribcage and lung segmentations. In contrast to the method described by Freyer et al.,<sup>48</sup> the initial position of the heart was not determined automatically but through user input, since, in our case, the typical thorax shape was deformed by squeezing in the imaging cartridge.

For the phantom study, only the tubes and the background medium were segmented from the complete volume since no other distinguishable structures were present. For segmentation purposes, the tube walls were employed as boundary indicators since they are visible with high contrast on the XCT images due to their different x-ray absorption characteristics over the phantom background medium. We manually selected the tube boundaries in two transversal slices of the XCT reconstruction, each at one end of the phantom, and used this input for automatic extraction of the rest of the tubes throughout the volume. All voxels lying inside the extracted tube walls were consequently assigned to the tube segments.

### 2.4 Phantom: Ex Vivo Imaging

Cylindrical, tissue mimicking phantoms with inclusions containing a NIR fluorescence dye with peak excitation at 679 nm

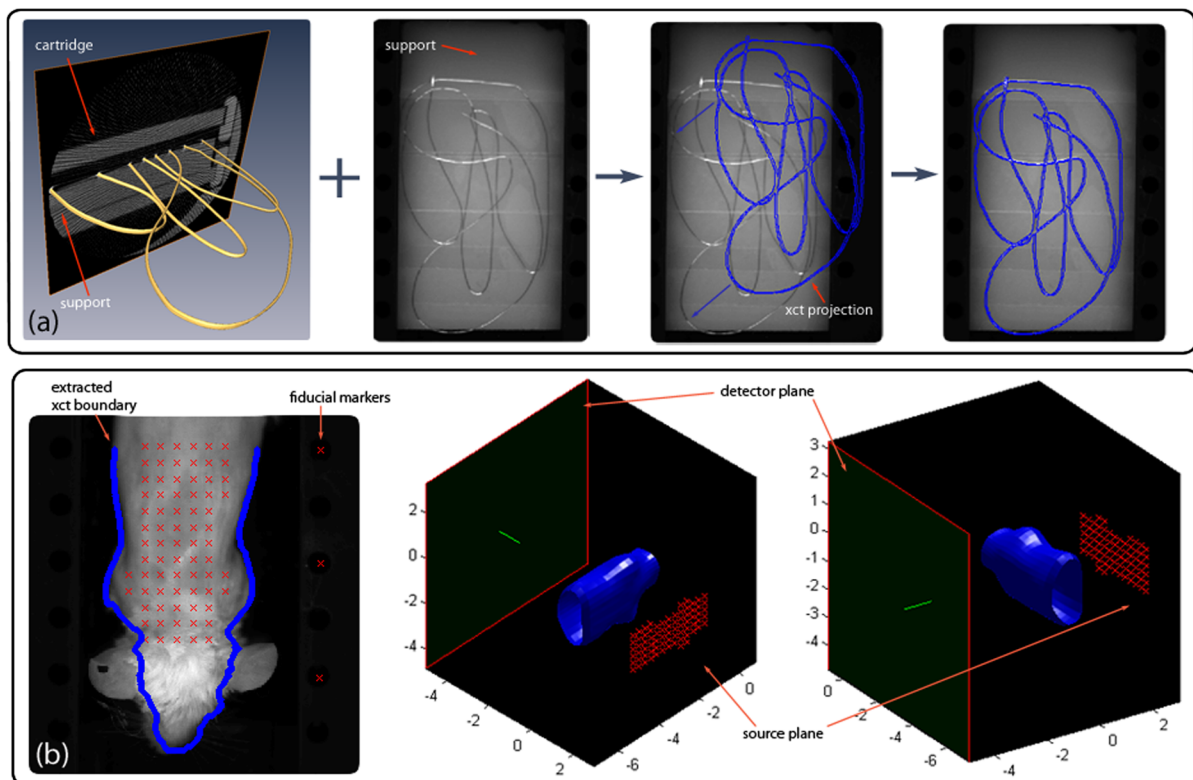


**Fig. 2** Co-registration approach: (a) The final accuracy of this approach was confirmed through imaging of a wire phantom. The XCT image (1st panel from left) and optical image (2nd panel from left) were co-registered and over-layed (3rd and 4th panel). (b) Fiducial markers and boundary mapping were used for the fusion of the FMT and XCT data sets (left). The source and detector information from the FMT device were projected on the boundary computed from the XCT (middle and right).

and peak emission at 702 nm (Alexa Fluor 680, Life Technologies Ltd., Paisley, United Kingdom) were imaged in both modalities. The phantoms were composed of a mixture of an adequate ratio of intralipid, ink, agar, and water in order to attain tissue properties of  $\mu'_s = 12 \text{ cm}^{-1}$  and  $\mu_a = 0.2 \text{ cm}^{-1}$  and were shaped to semi-cylinders resembling the shape of a mouse torso as illustrated in Fig. 1(a). The phantom measured approximately 36 mm in length and had a diameter of 30 mm at the widest point, the two inclusions had a diameter of approximately 3 mm. The tubes were positioned in the upper curved part of the semi-cylinder, as depicted in Fig. 1(a) by the red dotted circles and illustrated in more detail in Fig. 3 in the results section, and filled with the NIR fluorescent dye diluted in liquid with the same optical properties as the phantom, resulting in a fluorochrome concentration of 100 nMol.

## 2.5 In Vivo Imaging

Kras mice spontaneously developing tumors in the lung were used.<sup>49</sup> Approximately 24 h prior to imaging, a targeted fluorescence agent comprising an integrin  $\alpha_v\beta_3$  antagonist and a NIR fluorochrome with peak excitation at 675 nm and peak emission at 693 nm (IntegriSense 680, PerkinElmer, Waltham, Massachusetts) was administered via tail vein injection. At the beginning of the imaging session, the mice were anesthetized (Isoflurane 2%, O<sub>2</sub> 0.9 l/min) and placed in the previously described multimodal imaging cartridge that held the mouse motionless during the entire acquisition period in both FMT and XCT in a fixed position. First, x-ray CT was performed during approximately 10 to 15 min. Immediately following the XCT imaging session, FMT imaging was performed with a typical duration of 7 min. All procedures were performed in accordance with Helmholtz Center and Government of Bavaria law and regulations.

## 2.6 Ex Vivo Validation

Following *in vivo* imaging, the mice were euthanized by i.v. injection via catheter, of a lethal dose of a NaCl-Ketamine-Xylazine mixture, and frozen while still in the imaging cassette in order to keep their slightly squeezed shape for validation.

The mice were sliced in a cryotome (CM 1950, Leica Microsystems GmbH, Wetzlar, Germany) and each slice was imaged using an epi-fluorescence system at the according excitation/emission wavelength of 680/700 nm.<sup>50</sup> Images of *ex vivo* slices showing the true fluorescence distribution were compared to the corresponding reconstructed slices from the *in vivo* measurements as to their accordance in signal localization and relative signal intensity. This was done by defining, in the cryosections, a region around each tumor where a reconstructed signal would be admissible. Since the FMT reconstruction signal is more diffuse than the real signal, this region was chosen up to 2 mm around the actual tumor. The ratios of maximum fluorescence intensity in the tumor over maximum intensity in the muscle and in the lung were calculated for the cryosections. The same ratios were calculated for the *in vivo* data in the corresponding regions as determined from the cryosections. Generally, if the FMT reconstruction corresponds well to the *ex vivo* slices, the tumor/lung or tumor/muscle ratios should, ideally, linearly increase or decrease with increasing or decreasing cryoslice ratios.

The localization accuracy of the reconstructed fluorescence in the phantom was determined by defining concentric circles with increasing radius around the tubes and calculating the percentage of the total reconstructed signal per slice that was located inside the circles depending on the distance from the tube.

For validation of the fluorescence distribution in the mouse lung, we reconstructed a 3-D representation of the lung based on the lung cryoslices, using slices obtained every 250  $\mu\text{m}$ . This volume was interpolated to a voxel size of 50  $\mu\text{m}$  and rendered. By applying an intensity-based threshold at 50 percent of the maximum value observed (after shot-noise image filtering), a measure of fluorescence above background could be obtained for comparison with the FMT reconstruction.

## 2.7 Image Reconstruction

Stand-alone FMT reconstruction was based on a normalized Born approach previously published.<sup>51</sup> Incorporating XCT prior

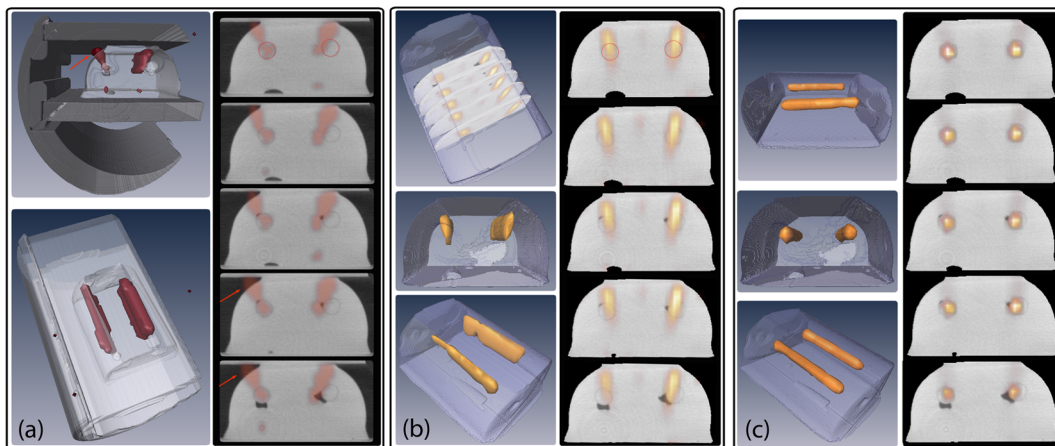


**Fig. 3** Phantom experiment showing reconstructions from the stand-alone FMT device (a) and hybrid approach (b and c). (a) Left: Three-dimensional (3-D) representation of the phantom with cartridge and adapter, showing the reconstruction provided by stand-alone FMT. In the lower image the fiduciary markers can be seen as red dots. Right: Slices through the reconstructed volume. (b) Left: 3-D view of the reconstructed fluorescence distribution using Tikhonov regularization. Here, only the outer boundary of the XCT was used in the reconstructions and no prior information was yet applied. The top image shows the position of the five slices that are shown in a, b and c. Right: Slices through the reconstructed volume. (c) Left: 3-D view of the reconstructed fluorescence distribution using differently weighted segments for regularization. Right: Slices through the reconstructed volume. The 3-D images were created using AMIRA software.

information into the FMT inversion code was based on a previously described algorithm which is briefly described here.<sup>40</sup>

Modeling of photon propagation in tissues was based on the diffusion equation, that is:

$$(-\nabla D \nabla + \mu_a) \Phi_f(r) = -n(r) \Phi_x(r), \quad (1)$$

where  $r$  is the spatial coordinate,  $\mu_a$  is the absorption coefficient,  $D$  is the diffusion coefficient [ $D = 1/(3\mu'_s)$ ,  $\mu'_s$  is the reduced scattering coefficient],  $n$  is a function proportional to the concentration of the fluorochrome and  $\Phi_x$  and  $\Phi_f$  describe the photon density at the excitation and emission wavelength, respectively. Equation (1) was implemented using a finite element solver for multiple source-detector pair measurements, which can be written in a simplified form as a linear matrix system:<sup>19</sup>

$$y = Wx, \quad (2)$$

where  $W$  is a  $N_{\text{measurements}} \times N_{\text{voxels}}$  matrix containing the weights (sensitivities) for every volume element (voxel) and each source-detector pair assumed, and  $y$  and  $x$  are vectors containing the normalized measurements and the unknown fluorescence distribution, respectively.

For the mouse study, different optical properties were assigned in the forward model to each of the segmented organs to take into account their varying level of scattering and absorption. They were experimentally determined for this mouse model and are listed in Ref. 52. For the phantom study, we used the same optical properties for all segmented regions, as described above. The difference in XCT and FMT resolution was taken into account by proportionally assigning each FMT voxel to its higher resolved anatomical segments as previously described in Refs. 33, 40, and 41.

Three ways of integrating anatomical data into the reconstruction of optical signals were considered in this study: the first did not use any information from the XCT but was based on boundary detection through the FMT camera, and further assumed slab geometry, due to the imposed shape of the imaging cartridge. Reconstructions based on this method were automatically provided from the used FMT imaging system. The second used the exact boundary detected by the XCT scan but no further anatomical information. The third fully integrated all available information from the XCT data, such as boundary and segmented organs. Consequently, depending on the different level of available anatomical information, different inversion schemes had to be implemented.

Inversion of Eq. (2), to solve for the unknown fluorescence image  $x$ , is an ill-posed problem which was solved herein by minimizing the residual of function  $F(x)$ :

$$F(x) = \|Wx - y\|^2 + \lambda \|Lx\|^2 \rightarrow \min!, \quad (3)$$

where  $L$  is called the regularization matrix and  $\lambda$  the regularization parameter which determines the order of influence of the penalty term  $\|Lx\|$  on the minimization problem. In this study, two types of regularization matrices were used which include the identity matrix ( $L = 1$ ) for implementing Tikhonov-type regularization (when no segmentation was used) and a diagonal matrix containing weights corresponding to different anatomical segments.<sup>40</sup>  $L$  equals the identity matrix when no prior information is implemented.  $L = I$  means that all voxels are equally regularized. Conversely, prior information can be implemented

by using an  $L$  matrix that contains different weights along its diagonal. These weights are employed to offer a different degree of regularization to different tissue structures (segments).

For inversion, we assigned the smallest weight ( $w_1 = 1$ ) to the lung region (for the *in vivo* measurements) and to the fluorescence tubes (in the phantom measurements). Reconstructed intensities appear smoother (more regularized) as the weight increases. For the mouse measurements, all other tissue regions segmented such as bones, heart, and remaining tissue assumed the same weight ( $w_2 = 4$ ).

This manual selection of weights is only appropriate when using phantoms or specific mouse models where the appearance of disease or fluorescence distribution is known beforehand.<sup>33,40</sup> This approach was also used, herein, for demonstration purposes with limited-projection-angle schemes using known phantoms and animal models. However, data-driven weight allocation is instead recommended to the more general case where the appearance of disease or the fluorochrome bio-distribution is not known beforehand.<sup>52</sup>

To determine the  $\lambda$  values, the minimization of Eq. (3) was solved for 200 different values of the regularization factor  $\lambda$ . Those values were chosen to be logarithmically spaced between  $10^{-6} * \|W\|$  and  $10^1 * \|W\|$ . An optimal  $\lambda$  value was then selected by  $L$ -curve analysis by plotting the solution norm versus the residual norm and then choosing the lambda value at the first corner of the resulting  $L$ -curve.<sup>53</sup> Following the  $L$ -curve analysis in which all optimal  $\lambda$  values of different data sets were found to be in a similar range, a common  $\lambda$  value was selected for all the reconstructions shown herein.

## 3 Results

### 3.1 Co-Registration Approach

Figure 2 shows the results obtained from the validation study examining the co-registration of FMT and XCT data.

Figure 2(a) shows an XCT image (1st panel from left) and a photograph (2nd panel from left) of the wire phantom as well as the overlay of both data sets after rotation, scaling and translation. The wire shape, extracted from XCT data and projected in one plane, could be perfectly aligned with the FMT reflectance image without any apparent nonoverlapping regions. The co-registration accuracy was measured as the distance between the wires as seen by the optical and the XCT image on the overlay of Fig. 2(a), 4th panel. This difference was found to be one pixel (worst case), i.e., max. 154  $\mu\text{m}$ , i.e., much smaller than the resolution achieved by FMT.

Figure 2(b) shows related results from animal imaging. The left panel depicts a black and white image of a mouse acquired with the FMT camera and the overlaid boundary extracted from the XCT image, shown in blue. The laser source positions and the location of the fiducial markers are projected onto the overlay in red. This projection is enabled by the integration of both modalities into one geometrical framework. The acquired fluorescence images could then, accordingly, be projected onto the same geometrical scheme.

### 3.2 Phantom Experiment

Figure 3 depicts results from the phantom measurements employed to further examine the accuracy of the registration approach and for comparing stand-alone reconstructions [Fig. 3(a)] to reconstructions using the XCT boundary [Fig. 3(b)]

and XCT tube segmentation [Fig. 3(c)]. Although the phantom had homogeneous optical properties and simplified internal boundaries compared to the complexity of tissue, the use of priors demonstrated regardless reconstruction improvement over reconstructions obtained in the absence of priors.

Figure 3(a) shows the reconstruction of the fluorescence signal assuming the phantom being an infinite homogeneous slab and without the use of priors (stand-alone reconstruction). The left column renders in gray 3-D x-ray CT images of the cassette and phantom inside the XCT scanner. Reconstructed fluorescence signals are co-registered on the images in dark red color. In the right column, transverse (axial) slices at different locations along the  $y$ -axis (as referred to in Fig. 1) are showing the localization of the reconstructed fluorescence signal inside the phantom. The location of the tubes can be seen on the XCT images and are highlighted in the first slice with red circles. Both in the upper image of the 3-D representation and in all transversal slices of Fig. 3(a), it can be observed that fluorescence distribution seen on stand-alone FMT reconstructions is partially located outside the real volume (highlighted by red arrows) and only partially coincides with the fluorescent inclusions.

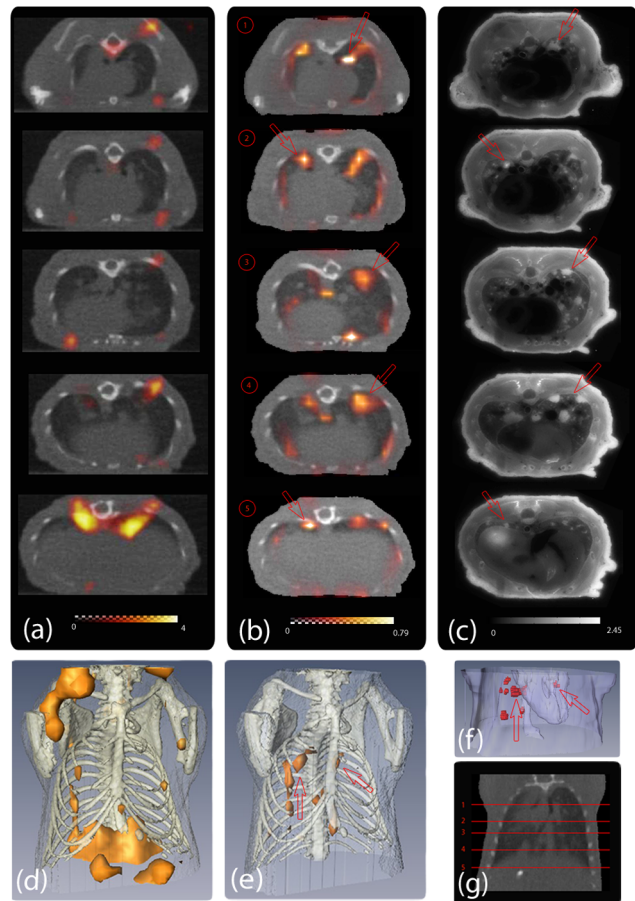
Figure 3(b) shows the corresponding reconstructions without priors, but using the actual phantom shape as boundary into the inverse code. The upper image in the left column shows the location of the five slices inside the phantom. The use of the boundary overall improves imaging performance, over stand-alone reconstructions in particular, along the horizontal axis [Fig. 2(b), right column]. On the vertical axis, both reconstructions reconstruct an elongated shape rather than a circle. The stand-alone reconstruction shows a displacement of the center of the ellipse toward the phantom boundary. Conversely, the use of the actual boundary better estimated the center of the fluorescence activity.

Figure 3(c), finally, depicts the reconstruction using the actual phantom boundary and anatomical priors. Here, additionally to the improved horizontal alignment, we can observe improved vertical alignment and confinement of the main fluorescence signal to the tubes.

### 3.3 In Vivo Imaging

Figure 4 depicts results from the *in vivo* studies. It compares stand-alone reconstruction using slab geometry and weighted segments reconstruction using priors in a lung tumor mouse model with *ex vivo* fluorescence images of the corresponding *in vivo* slices. The extraction of boundary information, and its incorporation into such optical imaging problems, was previously shown using other means like imaging with photogrammetric 3-D cameras or volume carving based on silhouette images.<sup>54,55</sup> The phantom study, additionally, showed best results when using priors. In this *in vivo* study, we, therefore, concentrated on the methodology and improvements specific to the hybrid FMT-XCT approach, namely through incorporation of priors due to organ segmentation.

The first column [Fig. 4(a)] shows stand-alone FMT reconstruction as it is output by the FMT 2500. In the second column [Fig. 4(b)], the reconstruction using weighted segments method is presented. Finally, the third column [Fig. 4(c)] contains *ex vivo* slices indicating the actual fluorescence intensity and distribution. The corresponding position in the mouse body can be seen in Fig. 4(g). All slices in one row but belonging to different columns correspond to each other.



**Fig. 4** Comparison of FMT reconstructions computed using stand-alone FMT without boundary or prior information (a) and hybrid FMT-XCT and the segmentation information derived from it (b) with corresponding *ex vivo* slices (c). All slices in one row are the same. The positions of the slices in each column are depicted in (g). 3-D representations of both stand-alone reconstruction (d) and hybrid reconstruction using priors (e) visualize the distribution and the fluorescent hot spots. The 3-D representation from the *ex vivo* slices (f) shows signals in the same spots as the hybrid reconstruction (e). All units are arbitrary. The 3-D images were created using AMIRA software.

The *ex vivo* validation images [Fig. 4(c)] show several areas with increased fluorescence intensity compared to surrounding lung tissue. Some examples are highlighted by red arrows. While, in some slices, only single outstanding points can be observed (e.g., slice 2) others show more than one above-average fluorescent signal source (e.g., slice 4). The hybrid reconstruction using priors [Fig. 4(b)] resolves the single fluorescence sources very well (e.g., arrows in slices 1 and 2) but seems not to be able to distinguish between three proximate but distinct spots (like in slice 4). Those are reconstructed as one single fluorescence source centered between the three source points.

The stand-alone method [Fig. 4(a)], in turn, allocates most of the reconstructed signal outside the lung tissue. Most of this distribution is, moreover, not in the expected region but above and below the lung.

As *in vivo* optical imaging achieves less resolution than the *ex vivo* validation method, reconstructed distributions can “irradiate” into adjacent tissue slices and appear there with less intensity. This can, for example, be observed in the third and fourth slice of the hybrid reconstruction [Fig. 4(b)]. The fluorescence signal in the middle of both (beneath the spine) only

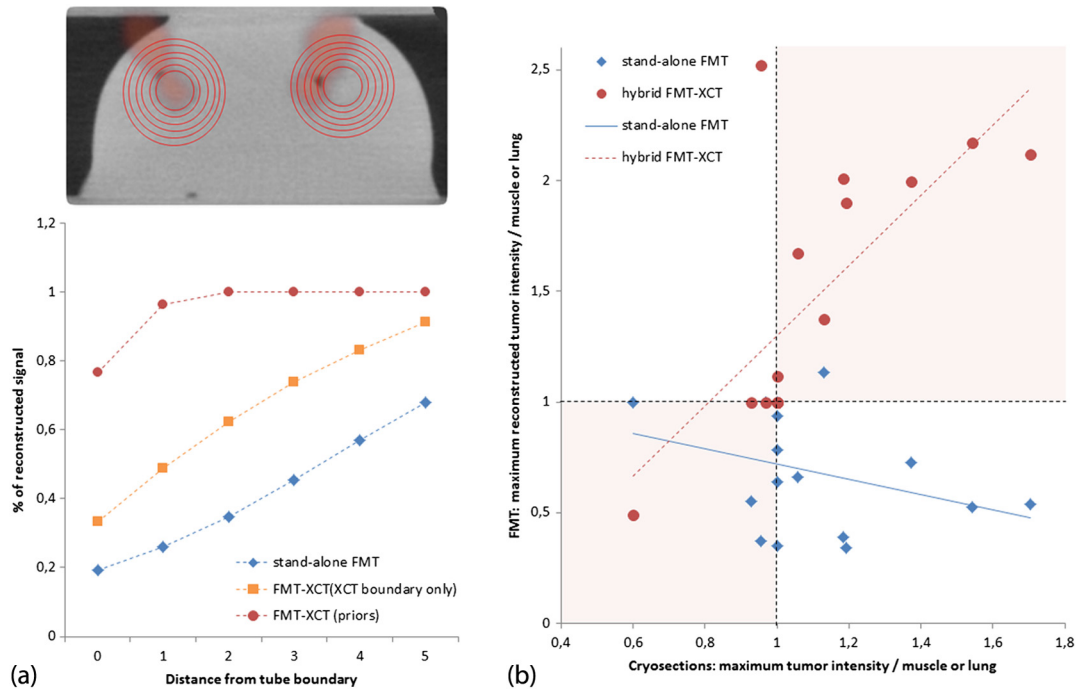


**Fig. 5** Comparison of reconstruction accuracy using the different reconstruction approaches in the phantom study (a) and in the *in vivo* study (b). (a): Plot of the percentage of reconstructed signal located inside a certain radius around the actual tube. (b): Plot of tumor/muscle and tumor/lung ratios in the *ex vivo* cryoslices versus *in vivo* stand-alone (diamond) and hybrid (dot) reconstructions.

appears in the fourth *ex vivo* slice and is quasi anticipated in the third slice of the hybrid reconstruction.

Note that due to the process of freezing and small displacements of the animal during this time, small shifts between *ex vivo* and *in vivo* images are expected and no utterly identical representation can be achieved.

Figure 4(d)–4(f), finally, show the 3-D view of the fluorescence distribution as to the *ex vivo* distribution [Fig. 4(f)], hybrid [Fig. 4(e)] and the stand-alone [Fig. 4(d)] reconstructions. Here, it becomes even more obvious where the main fluorescence signals in the stand-alone reconstruction are allocated. We applied a threshold to both 3-D representations in order to receive similar sized fluorescence signals in the lung. In the stand-alone case [Fig. 4(d)], this leads to proportionally higher signal intensities in those regions that were determined by the reconstruction to be the main fluorescence hot spots, such as around the shoulder and below the lung.

For the hybrid reconstruction, basically all areas are located inside the chest. This corresponds well to the *ex vivo* 3-D image, where the chest region around the heart [transparent structure inside the chest in Fig. 4(f)] is displayed. The most intense fluorescence spots are shown in red and arrows highlight the associated regions in Fig. 4(e) and 4(f).

### 3.4 Reconstruction Evaluation

Figure 5 evaluates the difference in reconstruction accuracy for the three reconstruction methods applied to *ex vivo* imaging [Fig. 5(a)] and the two reconstruction methods applied to *in vivo* imaging [Fig. 5(b)].

Figure 5(a) (top) shows one exemplary slice with the concentric circles at distances of 0 to 5 mm from the tube depicted in red. The innermost circle is at 0 mm distance from the tube which means that it represents exactly the tube boundary. Each

of the other circles has a distance of 1 mm from the other circles. The graph in Fig. 5(a) (bottom) shows the percentage of the recovered signal as a function of the distance from the tube for the stand-alone FMT (blue, diamond), FMT-XCT using only the boundary of the phantom (yellow, square) and FMT-XCT using priors (red, dot). Stand-alone FMT, thus, only localized 19 percent of the reconstructed signal inside the tube and, even in a distance of 5 mm around the tube, not more than 68 percent of the signal could be found. The reconstruction using the accurate mouse boundary and Tikhonov reconstruction recovered 33 percent of the signal inside the tubes and went up to 91 percent in a distance of 5 mm. The hybrid reconstruction using priors finally started with a localization of 77 percent inside the tubes and already reached 100 percent in a distance of 2 mm around the tubes.

For the evaluation of the reconstruction accuracy in the *in vivo* mouse study, we plot, in Fig. 5(b), the ratios of tumor/muscle and tumor/lung in the cryoslices versus the ratios of the same regions in the FMT reconstruction. In order to correlate with the *ex vivo* data, the *in vivo* data should, therefore, linearly increase with increasing cryoslices data. Therefore, acceptable data pairs would lie in the two quadrants highlighted in light red. It can be seen that almost all data pairs (92 percent) from the reconstruction using priors fulfilled this requirement and the general trend of the data showed a linear increase (red dots and dashed line). The reconstructions from the stand-alone FMT, in contrast, only plotted half of the data pairs inside the red quadrants (50 percent) and the trend line shows that the FMT signal was decreasing with increasing cryoslices signal (blue diamonds and continuous line).

## 4 Discussion

We investigated the imaging improvement achieved by limited-projection-angle FMT systems employing anatomical priors.

We found that the use of anatomical priors improves the imaging performance over stand-alone implementations, offering better image fidelity and superior quantification. Conversely, the use of priors requires the availability of a second tomographic modality imaging anatomy, for example an x-ray micro-CT system, an MRI system or ultrasound. Overall, this approach could “upgrade” a limited-projection-angle FMT device to offer more accurate molecular imaging performance.

Compared to 360 deg projections, limited-projection-angle FMT comes with manufacturing and operational simplicity and has been a preferred method in the biomedical laboratory. The availability of limited projection data, however, offer a challenging reconstruction problem, typically resulting in lower resolution and accuracy along the median axis of projections as evident on Figs. 3(a) and 4(a). This performance resembles the characteristics of limited projection x-ray tomosynthesis over x-ray CT, but in the diffusive photon regime.<sup>56,57</sup>

The use of prior information can reduce the ill-posed nature of the limited-projection-angle FMT inverse problem. The use of priors has shown to improve the imaging performance of 360 deg projection FMT, but it is even more essential for limited-projection-angle FMT, since reducing the information contained in the data collected increases the ill-posed nature of the reconstruction problem.<sup>52</sup> Our experimental findings, from the phantom measurements, showed that the image performance improves when using the actual boundary in the inversion, as compared to assuming the phantom being an infinite slab, a convenient theoretical approximation of early DOT approaches.<sup>45</sup> Naturally, the most accurate performance is found when anatomical priors of internal structures were also employed (Fig. 3).

The *in vivo* measurements corroborated these findings. *In vivo* data was confirmed by corresponding color and fluorescence imaging of cryoslices obtained *ex vivo*, serving, herein, as the “gold-standard.” It was found that reconstructed fluorescence signals were misplaced or erroneously allocated to areas outside the tissue volume, leading to imaging artifacts, when the inversion was performed with software that assumes the mouse as an infinite homogenous slab medium. In contrast, when the actual mouse boundary and anatomical priors were employed into the inversion code, the number of artifacts was significantly reduced and there were significant improvements in the congruency between *in vivo* data and fluorescence cryoslice images.

Nevertheless, limitations and requirements for algorithmic optimization were identified. Inversion with limited-projection-angle information may be more sensitive to estimates of the tissue optical properties, compared to 360 deg FMT systems. The particular inversion, employed herein, was based on the use of the normalized Born approximation, which offers a reconstruction problem that is insensitive to the variation of optical absorption, but which is still affected by the variation of scattering optical properties.<sup>58</sup> In this case, variations in the estimation accuracy of the underlying scattering properties of the various organs present in the tissue imaged may affect imaging accuracy. Measurement of the scattering properties of 3-D structures is not straightforward. In the context of using priors, such properties can be, in principle, retrieved by inversion of the light attenuation measurements obtained at different projections through the mouse. This can result in images offering a wavelength dependent optical property map. A further complication that arises in this case is that it is challenging to differentiate the scattering optical properties from the absorption optical properties when using constant light intensity (continuous wave) for

tissue illumination. Instead, in this study, we employed average tissue optical properties on a per organ level. This strategy has been shown to lead to moderate inaccuracy, when combined with image priors, for physiologically relevant under- or over-estimations.<sup>39</sup> This was confirmed in the data shown, herein, where congruence between *in vivo* reconstructions and cryoslicing data was obtained even with image reconstruction performed using optical property estimates. Future work should concentrate in further validating these assumptions with *in vivo* measurements and examine schemes where optical properties can be practically and accurately estimated on a per mouse basis.

As to the choice of accurate weights for the reconstruction using priors, further efforts will have to be made to develop completely data driven methods that are applicable to limited-projection-angle FMT. The choice of weights by the user can be adequate for studies as the ones presented herein, where well-known mouse models or phantoms were used for a proof of principle. In the more general case of biological investigation where, for example, the biodistribution of a probe in a certain mouse model is not yet known or the model itself is new and the disease progression to different parts of the body unclear, a manual weight selection is impossible and would lead to an inaccurate reconstruction. Although the introduction of weights will never influence the reconstruction as much as to introduce signals where there are none, it might, at least, smooth data too much in regions where it should not, thus, leading to a less localized and less quantitative result. Therefore, data-driven approaches, either based on Tikhonov reconstructions as previously described or on new methods based on, for example, a first low-resolution reconstruction, different segmentation or multi-spectral measurements need to be developed or refined.<sup>40,41</sup>

Overall, we found that the use of image priors significantly improves imaging performance in limited-projection-angle FMT. We believe that the complexity of utilizing data from another modality is well justified and counter-balanced by the accuracy improvement, which can extend the application versatility of limited-projection-angle FMT. The improvement in imaging performance, combined with the capacity of multiplexing using several probes at different wavelengths leads to potent molecular imaging performance surpassed possibly only by multi-spectral opto-acoustic tomography (MSOT).<sup>11</sup>

### Acknowledgments

The authors would like to thank Sybille Reder for her support with x-ray imaging and animal handling, and Sara Glasl and Florian Jürgeleit for their support with cryoslicing. The research leading to these results has received funding by the Deutsche Forschungsgemeinschaft (DFG), Sonderforschungsbereich-824 (SFB-824), subproject A1 and by the European Union Seventh Framework Programme under Grant Agreement No. [201792].

### References

1. V. Ntziachristos et al., “Looking and listening to light: the evolution of whole-body photonic imaging,” *Nat. Biotechnol.* **23**(3), 313–320 (2005).
2. R. Weissleder and M. J. Pittet, “Imaging in the era of molecular oncology,” *Nature* **452**(7187), 580–589 (2008).
3. U. Mahmood and R. Weissleder, “Near-infrared optical imaging of proteases in cancer,” *Mol. Cancer Ther.* **2**(5), 489–496 (2003).
4. R. Weissleder, “Scaling down imaging: molecular mapping of cancer in mice,” *Nat. Rev. Cancer* **2**(1), 11–18 (2002).

5. K. Shah and R. Weissleder, "Molecular optical imaging: applications leading to the development of present day therapeutics," *NeuroRx* **2**(2), 215–225 (2005).
6. S. Srinivasan et al., "Developments in quantitative oxygen-saturation imaging of breast tissue *in vivo* using multispectral near-infrared tomography," *Antioxid. Redox Signal.* **9**(8), 1143–1156 (2007).
7. B. Ballou et al., "Tumor labeling *in vivo* using cyanine-conjugated monoclonal antibodies," *Cancer Immunol. Immunother.* **41**(4), 257–263 (1995).
8. R. Weissleder et al., "*In vivo* imaging of tumors with protease-activated near-infrared fluorescent probes," *Nat. Biotechnol.* **17**(4), 375–378 (1999).
9. J. Haller et al., "Visualization of pulmonary inflammation using noninvasive fluorescence molecular imaging," *J. Appl. Physiol.* **104**(3), 795–802 (2008).
10. M. Nahrendorf et al., "Dual channel optical tomographic imaging of leukocyte recruitment and protease activity in the healing myocardial infarct," *Circ. Res.* **100**(8), 1218–1225 (2007).
11. V. Ntziachristos, "Going deeper than microscopy: the optical imaging frontier in biology," *Nat. Methods* **7**(8), 603–614 (2010).
12. R. Weissleder and V. Ntziachristos, "Shedding light onto live molecular targets," *Nat. Med.* **9**(1), 123–128 (2003).
13. S. R. Arridge, "Optical tomography in medical imaging," *Inverse Probl.* **15**(2), R41–R93 (1999).
14. J. Ripoll et al., "Kirchhoff approximation for diffusive waves," *Phys. Rev. E Stat. Nonlin. Soft. Matter. Phys.* **64**(5 Pt 1), 051917 (2001).\*\*\*
15. N. Deliolanis et al., "Free-space fluorescence molecular tomography utilizing 360 degrees geometry projections," *Opt. Lett.* **32**(4), 382–384 (2007).
16. M. J. Niedre et al., "Early photon tomography allows fluorescence detection of lung carcinomas and disease progression in mice *in vivo*," *Proc. Natl. Acad. Sci. U. S. A.* **105**(49), 19126–19131 (2008).
17. B. W. Pogue et al., "Hemoglobin imaging with hybrid magnetic resonance and near-infrared diffuse tomography," *Adv. Exp. Med. Biol.* **530**, 215–224 (2003).
18. V. Ntziachristos et al., "Concurrent MRI and diffuse optical tomography of breast after indocyanine green enhancement," *Proc. Natl. Acad. Sci. U. S. A.* **97**(6), 2767–2772 (2000).
19. R. B. Schulz et al., "Hybrid system for simultaneous fluorescence and x-ray computed tomography," *IEEE Trans. Med. Imaging* **29**(2), 465–473 (2010).
20. P. K. Yalavarthy et al., "Structural information within regularization matrices improves near infrared diffuse optical tomography," *Opt. Express* **15**(13), 8043–8058 (2007).
21. A. Li et al., "Optimal linear inverse solution with multiple priors in diffuse optical tomography," *Appl. Opt.* **44**(10), 1948–1956 (2005).
22. S. C. Davis et al., "Image-guided diffuse optical fluorescence tomography implemented with Laplacian-type regularization," *Opt. Express* **15**(7), 4066–4082 (2007).
23. Y. Lin et al., "Quantitative fluorescence tomography with functional and structural *a priori* information," *Appl. Opt.* **48**(7), 1328–1336 (2009).
24. R. L. Barbour et al., "MRI-guided optical tomography: prospects and computation for a new imaging method," *IEEE Comput. Sci. Eng.* **2**(4), 63–77 (1995).
25. M. Guven et al., "Diffuse optical tomography with *a priori* anatomical information," *Phys. Med. Biol.* **50**(12), 2837–2858 (2005).
26. D. W. Townsend, "Dual-modality imaging: combining anatomy and function," *J. Nucl. Med.* **49**(6), 938–955 (2008).
27. J. Ripoll et al., "Experimental determination of photon propagation in highly absorbing and scattering media," *J. Opt. Soc. Am. A Opt. Image Sci. Vis.* **22**(3), 546–551 (2005).
28. B. W. Pogue and K. D. Paulsen, "High-resolution near-infrared tomographic imaging simulations of the rat cranium by use of *a priori* magnetic resonance imaging structural information," *Opt. Lett.* **23**(21), 1716–1718 (1998).
29. X. Intes et al., "Diffuse optical tomography with physiological and spatial *a priori* constraints," *Phys. Med. Biol.* **49**(12), N155–N163 (2004).
30. A. Li et al., "Tomographic optical breast imaging guided by three-dimensional mammography," *Appl. Opt.* **42**(25), 5181–5190 (2003).
31. G. Gulsen et al., "Combined diffuse optical tomography (DOT) and MRI system for cancer imaging in small animals," *Technol. Cancer Res. Treat.* **5**(4), 351–363 (2006).
32. Q. Zhu et al., "Imager that combines near-infrared diffusive light and ultrasound," *Opt. Lett.* **24**(15), 1050–1052 (1999).
33. D. Hyde et al., "Hybrid FMT-CT imaging of amyloid-beta plaques in a murine Alzheimer's disease model," *Neuroimage* **44**(4), 1304–1311 (2009).
34. V. Ntziachristos et al., "MRI-guided diffuse optical spectroscopy of malignant and benign breast lesions," *Neoplasia* **4**(4), 347–354 (2002).
35. S. C. Davis et al., "MRI-coupled spectrally-resolved fluorescence tomography for *in-vivo* imaging," *Proc. SPIE* **6850** 68500K (2008).
36. F. Stuker et al., "Hybrid small animal imaging system combining magnetic resonance imaging with fluorescence tomography using single photon avalanche diode detectors," *IEEE Trans. Med. Imaging* **30**(6), 1265–1273 (2011).
37. X. Yang et al., "Combined system of fluorescence diffuse optical tomography and microcomputed tomography for small animal imaging," *Rev. Sci. Instrum.* **81**(5), 054304 (2010).
38. A. Da Silva et al., "Optical calibration protocol for an x-ray and optical multimodality tomography system dedicated to small-animal examination," *Appl. Opt.* **48**(10), D151–D162 (2009).
39. D. Hyde et al., "Performance dependence of hybrid x-ray computed tomography/fluorescence molecular tomography on the optical forward problem," *J. Opt. Soc. Am. A Opt. Image Sci. Vis.* **26**(4), 919–923 (2009).
40. A. Ale et al., "Imaging performance of a hybrid x-ray computed tomography-fluorescence molecular tomography system using priors," *Med. Phys.* **37**(5), 1976–1986 (2010).
41. D. Hyde et al., "Data specific spatially varying regularization for multimodal fluorescence molecular tomography," *IEEE Trans. Med. Imaging* **29**(2), 365–374 (2010).
42. X. Shu et al., "Mammalian expression of infrared fluorescent proteins engineered from a bacterial phytochrome," *Science* **324**(5928), 804–807 (2009).
43. N. Salem et al., "*In vivo* imaging of schistosomes to assess disease burden using positron emission tomography (PET)," *PLoS Negl. Trop. Dis.* **4**(9), e827 (2010).
44. T. Christen et al., "Molecular imaging of innate immune cell function in transplant rejection," *Circulation* **119**(14), 1925–1932 (2009).
45. E. E. Graves et al., "A submillimeter resolution fluorescence molecular imaging system for small animal imaging," *Med. Phys.* **30**(5), 901–911 (2003).
46. G. Zacharakis et al., "Fluorescent protein tomography scanner for small animal imaging," *IEEE Trans. Med. Imaging* **24**(7), 878–885 (2005).
47. M. Nahrendorf et al., "Hybrid *in vivo* FMT-CT imaging of protease activity in atherosclerosis with customized nanosensors," *Arterioscler. Thromb. Vasc. Biol.* **29**(10), 1444–1451 (2009).
48. M. Freyer et al., "Fast automatic segmentation of anatomical structures in x-ray computed tomography images to improve fluorescence molecular tomography reconstruction," *J. Biomed. Opt.* **15**(3), 036006 (2010).
49. L. Johnson et al., "Somatic activation of the K-ras oncogene causes early onset lung cancer in mice," *Nature* **410**(6832), 1111–1116 (2001).
50. A. Sarantopoulos, G. Themelis, and V. Ntziachristos, "Imaging the bio-distribution of fluorescent probes using multispectral epi-illumination cryoslicing imaging," *Mol. Imaging Biol.* **13**(5), 874–885 (2011).
51. V. Ntziachristos and R. Weissleder, "Experimental three-dimensional fluorescence reconstruction of diffuse media by use of a normalized Born approximation," *Opt. Lett.* **26**(12), 893–895 (2001).
52. A. Ale et al., "FMT-XCT: *in vivo* animal studies with hybrid fluorescence molecular tomography-X-ray computed tomography," *Nat. Methods* **9**(6), 615–620 (2012).
53. P. C. Hansen, "Analysis of discrete ill-posed problems by means of the L-Curve," *SIAM Rev.* **34**(4), 561–580 (1992).
54. R. B. Schulz, J. Ripoll, and V. Ntziachristos, "Experimental fluorescence tomography of tissues with noncontact measurements," *IEEE Trans. Med. Imaging* **23**(4), 492–500 (2004).
55. N. C. Deliolanis et al., "*In vivo* tomographic imaging of red-shifted fluorescent proteins," *Biomed. Opt. Express* **2**(4), 887–900 (2011).
56. J. T. Dobbins, 3rd and D. J. Godfrey, "Digital x-ray tomosynthesis: current state of the art and clinical potential," *Phys. Med. Biol.* **48**(19), R65–R106 (2003).
57. M. Rantala et al., "Wavelet-based reconstruction for limited-angle X-ray tomography," *IEEE Trans. Med. Imaging* **25**(2), 210–217 (2006).
58. T. Pyka et al., "Revisiting the normalized Born approximation: effects of scattering," *Opt. Lett.* **36**(22), 4329–4331 (2011).